Journal of Materials Chemistry A

ROYAL SOCIETY OF CHEMISTRY

PAPER

View Article Online
View Journal | View Issue

Cite this: J. Mater. Chem. A, 2022, 10, 3418

Delicate crystallinity control enables high-efficiency P3HT organic photovoltaic cells†

Kaihu Xian, [a] Yang Liu,[a] Junwei Liu,[a] Jinde Yu,[b] Yifan Xing,[b] Zhongxiang Peng, [a] Kangkang Zhou,[a] Mengyuan Gao,[a] Wenchao Zhao,[c] Guanghao Lu, [b] Jidong Zhang,[d] Jianhui Hou, [e] Yanhou Geng [af] and Long Ye *[agh]

As a benchmark semiconducting polymer, poly(3-hexyl-thiophene) (P3HT) has been broadly used to construct a wide range of organic electronic devices such as photovoltaic cells, photodetectors, thermoelectrics, and transistors. In the last two decades, numerous studies have concentrated on modulating the morphology and performance of organic solar cells based on P3HT and fullerene derivatives. In comparison with P3HT:fullerene systems, the blends of P3HT with emerging nonfullerene acceptors remain significantly less explored and the structure–performance relationships are not well established. In this work, time-dependent grazing incidence X-ray scattering and real-space microscopy experiments were carried out to monitor the microstructure change of the high-efficiency blend of P3HT and a Y6-type nonfullerene acceptor (*i.e.*, ZY-4Cl) over the duration of thermal annealing. By precisely manipulating the crystalline order of both the donor and acceptor, we found that simply shortening the annealing time can cause a remarkable 19-fold increase in the solar cell efficiency. We observed profound changes in all the photovoltaic parameters (open-circuit voltage, current density, fill factor, and power conversion efficiency) within the first 1 minute, while a slight variation emerged in the later stage. Attractively, the P3HT:ZY-4Cl blend film subject to thermal annealing for merely 30 seconds gave rise to a remarkable power conversion efficiency of ~10.7%, which is the best efficiency of P3HT-based organic photovoltaic cells at present. The research shed light on the morphological optimization and cost-effective processing of polythiophene:nonfullerene blends for optoelectronic applications.

Received 27th November 2021
Accepted 3rd January 2022

DOI: 10.1039/d1ta10161g

rsc.li/materials-a

1. Introduction

Solution-processed organic photovoltaic (OPV) cells are a clean energy technology with great commercial application prospects because of their unique features, such as high softness, light weight, colorful appearance and excellent ability to be translucent and wearable.[1–5] The past decade has witnessed dramatic advances in the performance of OPV cells and the reported power conversion efficiency (PCE) has surpassed 18%,[6–9] benefitting from the rapid development and innovation of new materials. However, the synthetic complexity and poor scalability of these new and high-efficiency materials result in considerably high production costs,[10–12] which put great constraints on the commercial development of OPVs. Therefore, more attention should be paid to optimizing low-cost polymer donors and nonfullerene acceptors with simple chemical structures and synthetic routes.[13–17]

Among the myriad of polymer donor materials, poly(3-hexylthiophene) (P3HT) is the lowest cost one due to its simple chemical structure and straightforward synthesis.[18,19] In particular, it can be readily made with some eco-friendly polymerization methods,[20–22] making P3HT the only polymer truly available in large quantities (over 1 kg). Limited by the narrow absorption range and intrinsically high-lying highest occupied molecular orbital (HOMO) level of P3HT, the photovoltaic performance of P3HT-based OPVs (denoted as P3HT-OPVs) is often far from satisfactory.[23,24] The PCE values of these cells are generally in the range of 7–9% even with a series of new

[a]School of Materials Science & Engineering, Tianjin Key Laboratory of Molecular Optoelectronic Sciences, Tianjin University, 300350 Tianjin, China. E-mail: yelong@tju.edu.cn

[b]Frontier Institute of Science and Technology, Xi'an Jiaotong University, Xi'an, 710054, China

[c]College of Materials Science and Engineering, Nanjing Forestry University, Nanjing 210037, China

[d]State Key Laboratory of Polymer Physics and Chemistry, Changchun Institute of Applied Chemistry, Chinese Academy of Sciences, Changchun 130022, China

[e]Beijing National Laboratory for Molecular Sciences, State Key Laboratory of Polymer Physics and Chemistry, CAS Research/Education Center for Excellence in Molecular Sciences, Institute of Chemistry, Chinese Academy of Sciences, Beijing 100190, China

[f]Joint School of National University of Singapore, Tianjin University, International Campus of Tianjin University, Binhai New City, Fuzhou 350207, China

[g]Songshan Lake Materials Laboratory, Dongguan, Guangdong 523808, China

[h]State Key Laboratory of Applied Optics, Changchun Institute of Optics, Fine Mechanics and Physics, Chinese Academy of Sciences, Changchun 130033, China

† Electronic supplementary information (ESI) available. See DOI: 10.1039/d1ta10161g

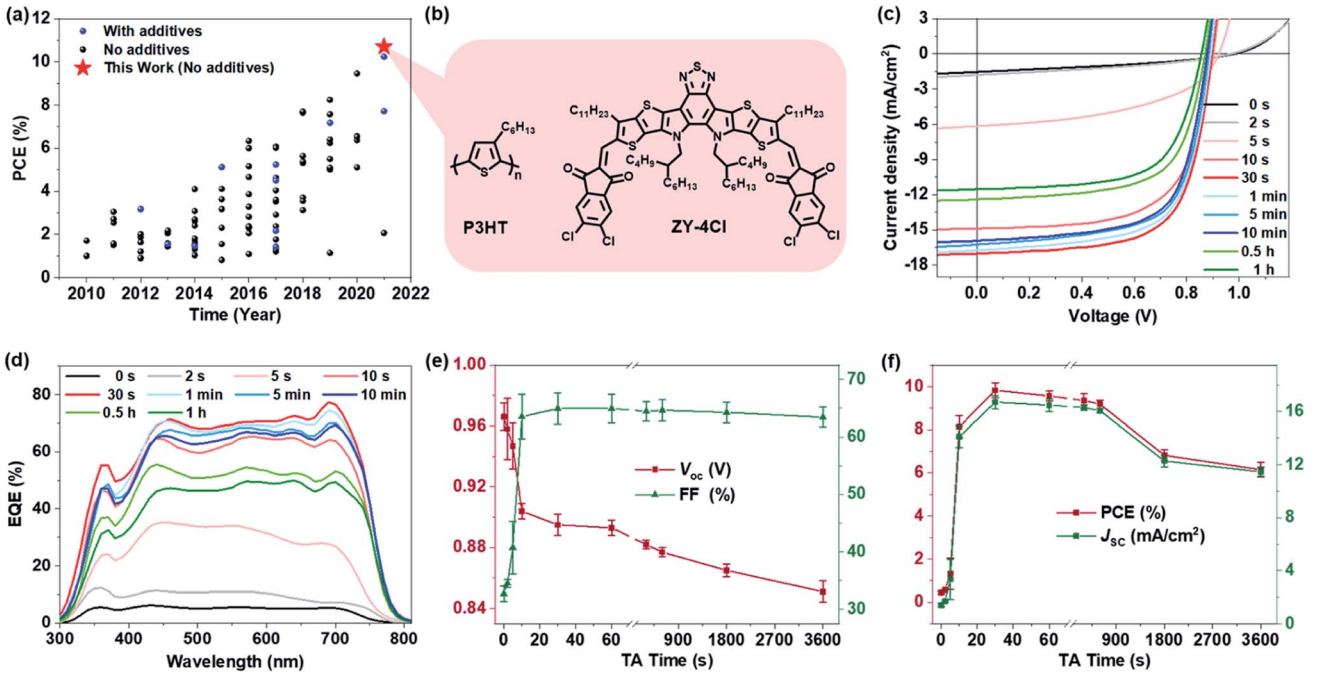

Fig. 1 (a) Summary of the PCEs for nonfullerene P3HT-OPVs with and without additives. The value achieved in our study is marked with a star. (b) Chemical structures of the model blend system of P3HT and ZY-4Cl. (c) *J*–*V* curves of the optimal P3HT:ZY-4Cl blend films with different annealing times. (d) EQE curves of the corresponding devices. The evolution plots of (e) V_{OC} and FF, and (f) J_{SC} and PCE with annealing time.

nonfullerene acceptors[25] such as O-IDTBR[26] and TrBTIC[27] (see Fig. 1a). The best PCE of P3HT-OPVs is no more than 9% unless the state-of-the-art Y6 type nonfullerene acceptor (*i.e.*, ZY-4Cl[28]) is employed. Though these P3HT:nonfullerene blends are still less efficient compared with the high-efficiency OPV systems, the innovations in molecular structure design of nonfullerene acceptors have still provided a lot of new opportunities for device optimization and demonstrated the huge potential of P3HT-OPV systems.[29–32]

Compared with fullerene derivatives, non-fullerene acceptors can continuously adjust the molecular energy level and band gap through chemical structure modification, realize the utilization of photons at different wavelengths and thus enable more excellent performance.[33–35] In 2015, McCulloch's group developed a rhodanine flanked nonfullerene small molecule acceptor, FBR, enabling a PCE of 4.11%,[36] which was the first time that P3HT-OPVs based on nonfullerene acceptors outperformed their fullerene counterparts. Furthermore, they replaced the fluorene core of FBR with indacenodithiophene and synthesized two benzothiazole derivatives, O-IDTBR and EH-IDTBR,[37] to address the issues of spectral overlap and morphologies from FBR. Since a more planarized molecular structure leads to complementary absorption and suitable crystallinity, P3HT-OPVs based on O-IDTBR and EH-IDTBR showed PCEs of 6.34 and 6.00%, respectively. In 2019, Han's group used 1,2,4-trichlorobenzene as an additive to separate the crystallization process of P3HT and O-IDTBR by extending the film-forming duration and increased the PCE of the P3HT:O-IDTBR blend to 7.18%.[26] In the same year, Peng *et al.* synthesized a new nonfullerene acceptor named TrBTIC,[27] which crystallized slowly with long-term aging in 1,2,4-trimethylbenzene at room temperature. The P3HT:TrBTIC film showed a PCE of 8.25% due to the phase separation of the donor and acceptor with long-term aging before spin-coating.

In addition to manipulating the microstructure of the blend films by modulating the solution properties and film-forming processes, the morphology can also be adjusted after film formation by post-treatments. Recently, Hou and co-workers found that the photovoltaic performance of a new P3HT:nonfullerene film reaches 9.46% by a standard thermal treatment (for instance, heating at 130 °C for 10 min), which significantly outperformed the control device without annealing. In a subsequent report, Hou *et al.* introduced a small amount of volatilizable solid additive to form a more ordered molecular packing for a nonfullerene acceptor and obtained a respectable PCE greater than 10%,[38] which broke the prior efficiency record for P3HT-OPVs. These studies together indicated that the morphology of the blend films is quite sensitive to the processing conditions.[39–41] Nevertheless, the knowledge of how the morphology of the P3HT:nonfullerene blend film evolves over the course of post-treatment (*e.g.*, annealing) is still scarce and has remained an extremely challenging task for morphology control in the field. As such, understanding the morphological details of P3HT:nonfullerene films and their evolution with post-treatment time is of vital importance to rationalize the optimization strategies with a view to a greater performance in P3HT-OPVs.

Here we have successfully surpassed the 10% efficiency barrier for additive-free P3HT-OPVs with a facile strategy and importantly managed to finely monitor the time-dependent evolution of crystallization, morphology and photovoltaic

performance of a low-cost yet high-efficiency OPV active layer during the thermal annealing process. Our model system (see Fig. 1b) is representative of the recently emerging polythiophene:nonfullerene blends, consisting of the Y6-series small molecule acceptor ZY-4Cl (2,2′-((12,13-bis(2-butyloctyl)-3,9-diundecyl-12,13-dihydro-[1,2,5]thiadiazolo[3,4-e]thieno[2″,3″:4′,5′]thieno[2′,3′:4,5]pyrrolo[3,2-*g*]thieno[2′,3′:4,5]thieno[3,2-*b*]indole-2,10-diyl)bis(methaneylylidene))bis(5,6-dichloro-1*H*-indene-1,3(2*H*)-dione)) and the optimal batch of P3HT that was prepared by our direct arylation polycondensation protocol.[42] It was found that the amorphous portion of acceptors crystallized rapidly in a short period (30 s) and then agglomerated with the further extension of annealing time, while the crystallinity of P3HT did not change substantially after annealing. Therefore, the phase separation of the blends increased gradually with prolonged annealing time. We demonstrated that the crystallization of photoactive materials can significantly improve the device performance, but the agglomeration of crystallized acceptor molecules will hamper the performance. By thermally annealing the blend film for only 30 s at 130 °C without extra liquid or solid additives, we were able to achieve an impressive PCE of 10.71%, which is the record PCE value of P3HT-OPVs. By precisely optimizing the crystalline order of both the donor and acceptor *via* shortening the annealing time, we demonstrated a remarkable 19-fold increase in the solar cell efficiency. We found that higher efficiency can be achieved in a very short time in comparison with that of the films normally annealed for 10 min. This facile strategy has a great advantage over the previously reported ones in terms of lowering the cost and time of industrial production of P3HT solar cells. It will provide guidance for the regulation of the aggregated structure of films, so as to advance the performance improvement of polythiophene solar cells.

2. Results and discussion

2.1. Photovoltaic performance

To examine how photovoltaic parameters evolve with the processing conditions, we constructed a series of OPVs with a conventional structure of ITO glass/PEDOT:PSS/P3HT:ZY-4Cl/PDINO/Al, by simply altering the annealing time of the active layer at 130 °C. The processing solvent is tetrahydrofuran, which is widely recognized as a sustainable solvent. The detailed fabrication conditions are provided in the ESI.† The energy level alignments are illustrated in Fig. S1.† The current density–voltage (*J*–*V*) curves of the blends under AM 1.5G conditions (100 mW cm^{-2}) are shown in Fig. 1c and the detailed photovoltaic parameters are summarized in Table 1. The as-cast (0 s) device gave an abysmal PCE of 0.51% with a high open-circuit voltage (V_{OC}) of 0.98 V, a poor short-circuit current density (J_{SC}) of 1.5 mA cm^{-2} and a low fill factor (FF) of 0.35. In comparison, the device with thermal annealing for 10 min afforded a notably raised PCE of 9.37% with a lower V_{OC} of 0.88 V, a good J_{SC} of 15.9 mA cm^{-2} and a high FF of 0.67. Intriguingly, after only thermal annealing for 30 s, we achieved the peak PCE of 10.25% with a V_{OC} of 0.90 V, a J_{SC} of 17.0 mA cm^{-2} and a FF of 0.67. The champion PCE achieved here is the highest value reported so far for P3HT-OPVs. Of particular note is that our high-performance P3HT-OPV does not require the use of any extra liquid or solid additives.

As displayed in Fig. 1d, the external quantum efficiency (EQE) value of the as-cast blend film was lower than 5% in the entire response region of 300–800 nm. The blend films annealed for 30 s exhibited significantly stronger photoresponses with the maximum EQE exceeding 70%. The deviations between the calculated integrated current densities from the EQEs and the J_{SC} obtained from the *J*–*V* measurements were less than 5% for all the devices, demonstrating the reliability of our solar cell performance. As can be seen from Fig. 1e, there was an 80 mV sharp decline in V_{OC} after thermal annealing at 130 °C within 10 s, and then the V_{OC} decreased slowly with annealing time. As reflected in the FF plot, it increased rapidly with annealing time in the first 10 s and then appeared to level off. As shown in Fig. 1f, the J_{SC} quickly increased to a peak value within 30 s and then a slow decrease in J_{SC} with annealing time was recorded after 30 s. The PCE first increased rapidly and then decreased slowly, exhibiting an analogous trend with J_{SC}. The performance change during the annealing process can be understood by further mapping out the evolution of the crystallization and morphology of the blend films over time.

Table 1 Detailed photovoltaic parameters of the P3HT-OPV cells as a function of annealing time at 130 °C under AM 1.5 G illumination

Time	V_{OC} (V)	J_{SC} (mA cm^{-2})	J_{cal}[a] (mA cm^{-2})	FF	PCE[b] (%)
0 s	0.97 ± 0.01 (0.98)	1.4 ± 0.1 (1.5)	1.2	0.33 ± 0.01 (0.35)	0.44 ± 0.05 (0.51)
2 s	0.96 ± 0.02 (0.97)	1.7 ± 0.1 (1.8)	2.3	0.35 ± 0.01 (0.35)	0.57 ± 0.02 (0.61)
5 s	0.95 ± 0.02 (0.92)	3.3 ± 1.5 (6.1)	7.0	0.41 ± 0.04 (0.49)	1.32 ± 0.72 (2.75)
10 s	0.90 ± 0.01 (0.90)	14.1 ± 0.8 (14.9)	14.7	0.64 ± 0.04 (0.64)	8.14 ± 0.52 (8.58)
30 s	0.90 ± 0.01 (0.90)	16.7 ± 0.5 (17.0)	16.7	0.65 ± 0.03 (0.67)	9.83 ± 0.35 (10.25)
1 min	0.89 ± 0.01 (0.89)	16.5 ± 0.2 (16.7)	16.3	0.65 ± 0.02 (0.66)	9.57 ± 0.23 (9.81)
5 min	0 88 ± 0.00 (0.88)	16.3 ± 0.2 (16.3)	15.8	0.64 ± 0.02 (0.67)	9.35 ± 0.34 (9.61)
10 min	0.88 ± 0.00 (0.88)	16.1 ± 0.2 (15.9)	15.5	0.65 ± 0.02 (0.67)	9.19 ± 0.19 (9.37)
0.5 h	0.87 ± 0.00 (0.87)	12.3 ± 0.5 (12.4)	12.4	0.64 ± 0.02 (0.65)	6.82 ± 0.25 (7.01)
1 h	0.85 ± 0.01 (0.86)	11.5 ± 0.3 (11.5)	11.3	0.63 ± 0.02 (0.65)	6.15 ± 0.34 (6.43)
30 s[c]	0.90 ± 0.01 (0.90)	17.1 ± 0.4 (17.4)	16.9	0.66 ± 0.04 (0.69)	10.15 ± 0.48 (10.71)

[a] J_{cal} is calculated from the EQE curve. [b] The average values of the photovoltaic parameters are obtained from 10 devices. [c] The values are obtained by using a new P3HT batch with 95% regioregularity.

2.2. Crystalline order

Since the performance changed sharply during the thermal processing, we applied a synchrotron radiation-based X-ray diffraction technique, namely grazing incidence wide-angle X-ray scattering (GIWAXS), to characterize the crystalline order and texture of the blend films. As shown in the time-dependent evolution diagrams of neat P3HT by GIWAXS (Fig. S2†), the out-of-plane diffraction peak at 0.39 $Å^{-1}$ corresponds to the (100) reflection from the alkyl-stacking direction of the P3HT crystallites.[43] Upon annealing, the neat P3HT films showed very analogous diffraction profiles. More specifically, the as-cast film showed significantly small coherence lengths (L_c) and peak areas of the (100) and (010) peaks, which indicated that although a small portion of P3HT is crystalline in the as-cast film, most of the polymer chains are still in a disordered state. After annealing, we observed the enhanced crystallinity of P3HT. Two weak peaks appeared at $q_z = 0.77$ and 1.16 $Å^{-1}$ after annealing, which can be assigned to the (200) and (300) reflections. The peak at $q_z = 1.67$ $Å^{-1}$ can be assigned to the (010) π–π stacking reflection. L_c was calculated using the Scherrer equation[44] of diffraction peaks: $L_c = 2\pi k/\Delta q$, where k is the dimensionless shape factor (herein $k = 0.9$) and Δq is the full width at half maximum (FWHM) of the given peak (Table S1†). The L_c of the (100) reflection increased rapidly at first and then slowly, while the L_c of the (010) reflection increased rapidly and then leveled off, suggesting the strengthening of P3HT order in the alkyl-stacking.

Different from fullerene derivatives, nonfullerene acceptors exhibited much more complex aggregation characteristics and often crystallized in various crystalline forms.[45–48] However, our attempts to capture crystalline signals by growing single crystals of ZY-4Cl or differential scanning calorimetry (DSC) measurements failed, which prevented implementing a more detailed analysis of its polymorphism. As shown in Fig. S3 and Table S2,† we can still observe that ZY-4Cl molecules are in an amorphous state in the as-cast film. As annealing treatment activated the movement of acceptor molecules, ZY-4Cl crystallized quickly and there were multiple polymorphs formed at the same time. The polymorph formation was instantaneously completed (within 10 s) after thermal activation and further annealing did not affect the crystal orientation and extent obviously.

Fig. 2 depicts the stacking evolution diagrams of blend films with annealing time measured by GIWAXS. Table S3† summarizes the position and L_c of different peaks. The diffraction peaks at ~0.39 and 0.76 $Å^{-1}$ can be assigned to the reflection of P3HT and those at 0.31, 0.52, 0.63, 1.34, 1.53 and 1.82 $Å^{-1}$ can be assigned to the reflection of ZY-4Cl. The movement of the donor and acceptor in the blend film will affect each other. Although the formation of ZY-4Cl polycrystals with annealing is carried out at the same time, the different diffraction signals are gradually observed on different time scales. The as-cast blend film exhibited a very weak π–π stacking diffraction at 1.67 $Å^{-1}$, which arises from both P3HT and ZY-4Cl. A diffraction peak at ~0.39 $Å^{-1}$ could be observed after annealing for 2 s. The heat received by the film annealed for 2 s is so limited that the properties and microstructure are almost the same as those of the as-cast film, due to the poor heat conductivity of the substrate. Two diffraction peaks at ~0.62 and 1.83 $Å^{-1}$ could be observed after annealing for 5 s. This implies that ZY-4Cl has started to crystallize under thermal activation. Three diffraction peaks at ~0.52, ~1.33 and ~1.53 $Å^{-1}$ could be observed if the annealing time increased up to 10 s. All of the diffraction peaks attributable to ZY-4Cl have been observed at this time. Upon annealing, the intensity of these peaks evolved and exhibited a rapid increase in the first few seconds. This phenomenon also provided strong proof of the fast thermally activated kinetic process after annealing in the blend films. Further annealing improves thin-film crystallinity and a fast increase in J_{SC} was recorded. The intensity of diffraction peaks can reflect the degree of molecular orientation in the blend films. The intensities of all diffraction peaks, in both out-of-plane and in-plane directions (Fig. S4†), reached the maximum after annealing for 30 s. It demonstrates that the molecular order in the device annealed for 30 s is the highest, thus affording the best photovoltaic performance.

A diffraction peak at ~0.56 $Å^{-1}$ and some very faint spurious peaks could be observed when the annealing time was extended to 0.5 h. These diffraction peaks are not observed in the neat donor and acceptor films, indicating that long-term annealing makes the distribution of aggregation structure chaotic and even forms different types of aggregate. For instance, the reflection peaks at $q = 0.56$ $Å^{-1}$ become much stronger when a longer time (>30 min) of annealing is applied. The multiple peaks for the blend films might not only be due to ZY-4Cl movement but also originate from the molecular interactions between P3HT and ZY-4Cl. Two diffraction peaks at ~0.31 and 0.76 $Å^{-1}$ could be observed when the annealing time is extended to 1 h. The (200) diffraction peak of P3HT can be observed, indicating that the crystalline order of P3HT increased continuously with annealing. The crystallization of P3HT and ZY-4Cl could be gradually strengthened by continuous annealing.

2.3. Phase separation

Having determined that the performance and crystalline order of the P3HT:ZY-4Cl blend films are sensitive to the processing time, we proceeded to probe the morphological difference with real-space microscopy. The surface morphologies of the P3HT:ZY-4Cl-based blend films with the increase of annealing time were investigated by atomic force microscopy (AFM), operating in tapping mode. All the blend films were prepared under the same conditions as those used for the fabrication of the optimal devices. As presented in Fig. 3, the as-cast P3HT:ZY-4Cl film possessed a root-mean-square surface roughness (R_q) of 0.80 nm and a homogeneous granuliform surface similar to that of the neat P3HT film (Fig. S5†). The morphology of the film annealed for 2 s is consistent with that of the as-cast film.

Based on the AFM images of the neat films, we found that the aggregation enhancement of P3HT with annealing time is inconspicuous compared to that of the ZY-4Cl. Neat P3HT films exhibited a granular and uniform appearance with the R_q value slightly increasing from 0.62 to 0.92 nm by annealing. In contrast, the crystallinity of ZY-4Cl has been greatly improved after annealing, resulting in a significantly larger domain size

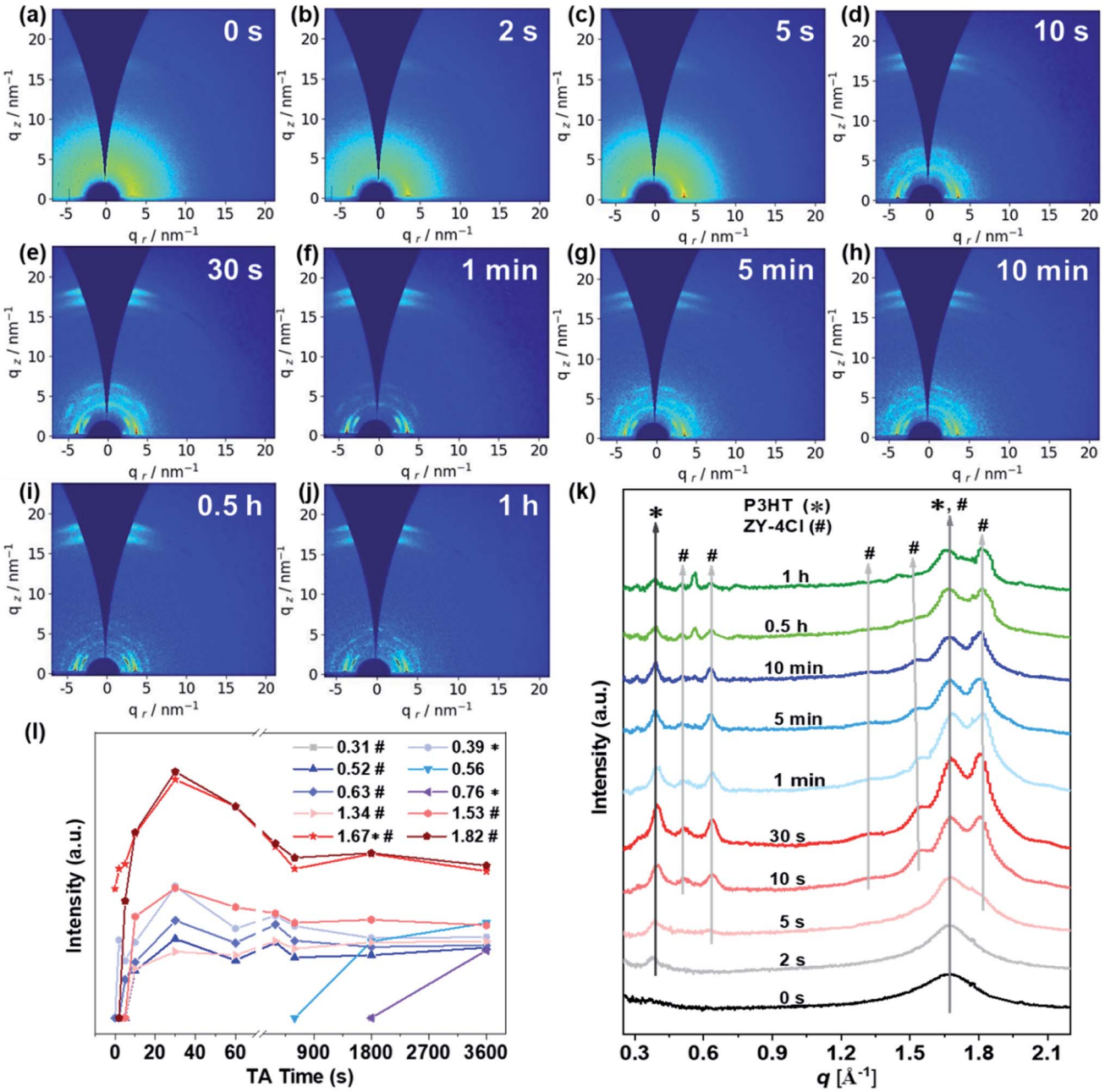

Fig. 2 (a–j) The time-dependent evolution of the 2D GIWAXS patterns of the P3HT:ZY-4Cl blend films with annealing time. (k) The corresponding out-of-plane sector-averaged profile for all of the blend films. (l) The intensity of all diffraction peaks with annealing time. The marks represent the characteristic diffraction reflections of P3HT and ZY-4Cl. Note that * denotes the diffraction features of P3HT and # represents the reflection peaks of ZY-4Cl.

and the R_q value increases obviously from 0.40 to 3.82 nm, which represents the conspicuously larger size of the acceptor domain. It demonstrates that there is strong self-aggregation of ZY-4Cl molecules.

The particle aggregation of the blend films becomes more pronounced after annealing for 5 s. Due to the poor crystallinity of ZY-4Cl at this time (as supported by its neat film data), the particle aggregation is mainly caused by the crystal formation and enhanced crystallinity of P3HT. With the enhanced crystallinity of ZY-4Cl when annealing for 10 s, ZY-4Cl crystals are mixed into the P3HT chains, which reduces graininess on the film surface and makes the film surface smoother. At the same time, the enhancement of the crystallinity of ZY-4Cl crystals also makes the blend film form a better phase separation structure.

As the crystallinity of P3HT and ZY-4Cl increases with prolonged annealing, the film interface becomes clearer accompanied by a gradually increasing R_q value. To attain the size scale of phase separation, the power spectral density (PSD) profiles were obtained by fast Fourier transform analysis of AFM phase images (Fig. S6 and Table S4†). The approach of attaining

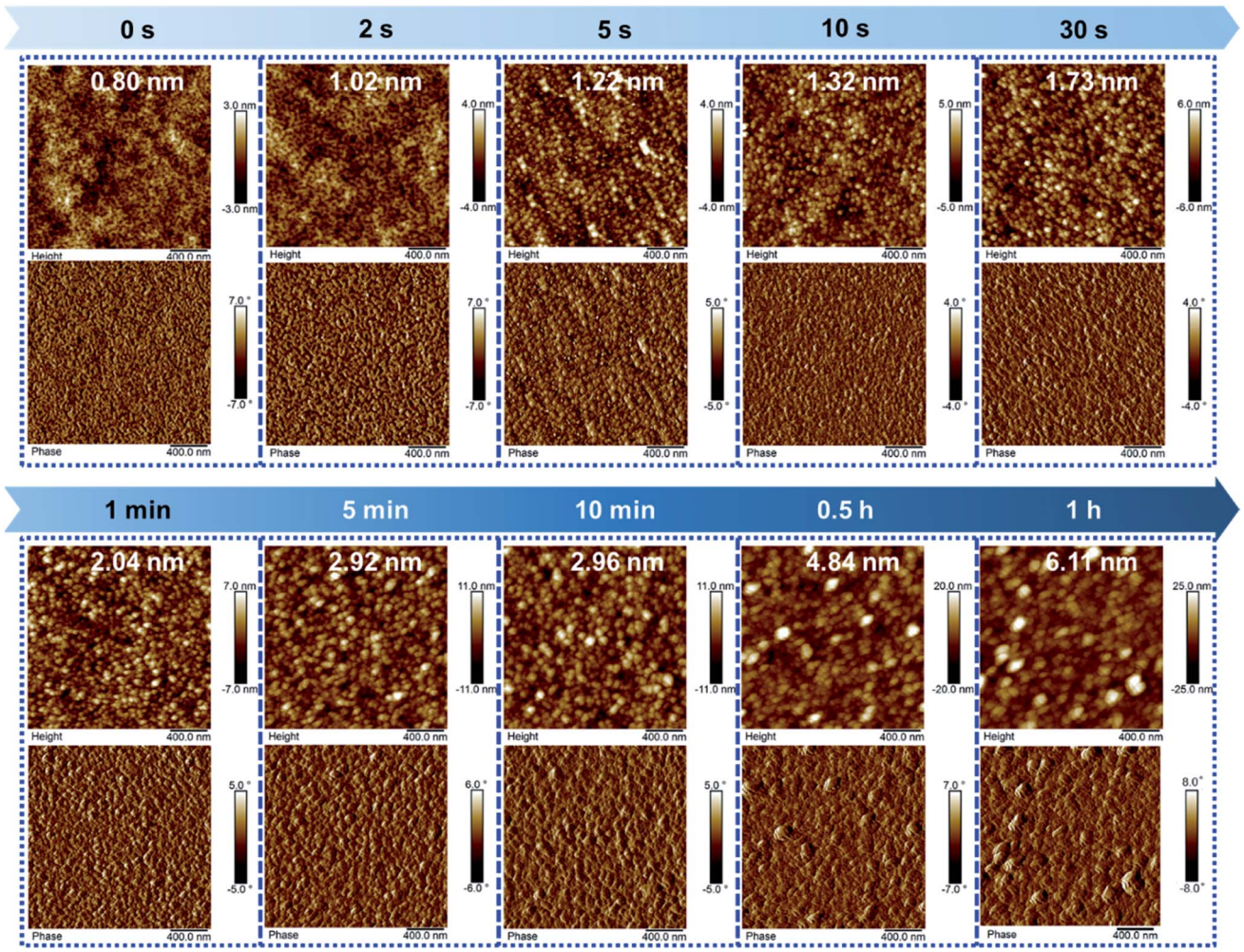

Fig. 3 The evolution of AFM height and phase images of all blend films with annealing time ranging from 0 s to 1 h. The R_q data are listed.

PSD profiles has been well utilized and documented in organic/polymeric electronic films.[49,50] The results indicated that the characteristic domain spacing of the blend films gradually increases with annealing time. The best phase separation within the blend film was obtained after annealing for 30 s with a modest R_q of 1.73 nm.

Upon further increasing the annealing time (to more than 5 min), island-like agglomerations appeared gradually on the surface of the films. In addition, as evidenced from the transmission electron microscopy (TEM) images (Fig. S7a–c†), the island-like agglomerations become enlarged and more extensive with long-term annealing within the entire film. Considering that P3HT-containing blend films often show vertically phase-separated morphology,[51,52] *in situ* film-depth dependent light absorption spectroscopy (FLAS) measurements were conducted.[53] In particular, we quantitatively monitored the vertical profiles of each component across the whole thickness of the relevant active layers (Fig. S7d†). We can easily find that there is no obvious vertical phase separation in the P3HT:ZY-4Cl film. Therefore, the analysis of this phenomenon obtained from the surface of the films is applicable within the entire film space. This is a thermodynamically driven spontaneous process resulting from Ostwald ripening.[54] The crystallized small molecule acceptor ZY-4Cl appears to be a kind of nanoparticle. Usually, large nanoparticles, with their lower surface to volume ratios, result in a lower surface energy. Thus, larger nanoparticles are more energetically stable than smaller nanoparticles. Subsequently, molecules on the surface of a small nanoparticle will tend to detach and diffuse and then attach onto the surface of a larger nanoparticle. Therefore, the number of smaller nanoparticles continues to shrink, while that of larger nanoparticles continues to grow. In this work, the heat during annealing provides kinetic energy for the movement of ZY-4Cl nanoparticles and the acceptors aggregate through more rapid and long-range diffusion in the blend film. The excessive agglomeration of ZY-4Cl results in strong demixing of the active blend and even perturbs the crystallinity. It will destroy the original interpenetrating network structure, not conducive to exciton dissociation and carrier transport.

2.4. Optical absorption

As a complement to the above crystallization characterization, we examined the aggregation behaviors of the two neat components P3HT and ZY-4Cl by acquiring the ultraviolet-

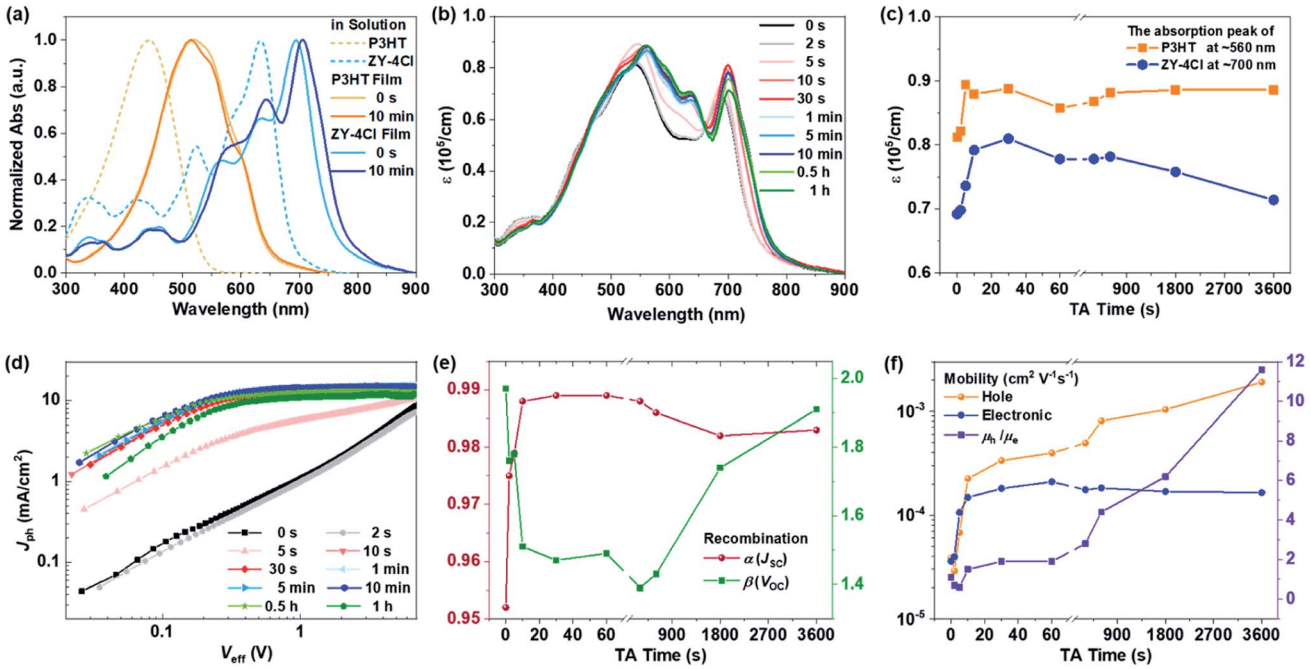

Fig. 4 (a) UV-vis absorption spectra of P3HT and ZY-4Cl in diluted THF solutions and films. (b) UV-vis absorption spectra of the blend films based on P3HT:ZY-4Cl. (c) The evolution of absorption coefficients at ~560 and 700 nm during the thermal annealing process. (d) J_{ph} *versus* V_{eff} plots of all devices as a function of annealing time. (e) Recombination evolution plots of α and β values from light intensity dependence measurements. (f) Hole and electron mobility evolution plots with annealing time.

visible (UV-vis) absorption spectra in THF solutions and films. As shown in Fig. 4a, P3HT in dilute THF solution exhibited a characteristic absorption peak at 443 nm. This absorption peak is related to the π–π* transition of P3HT. In hot (50 °C) solution, the molecular chains present a relatively extended random coil conformation affected by thermal fluctuations. From solution to film, the aggregation of molecular chains increases the planarization degree and effective conjugate length, improves the electron delocalization degree, and reduces the band gap, which together makes the absorption peak red-shift by 72 nm. At the same time, the molecular crystallization causes two weak characteristic absorption peaks of π–π stacking near 540 and 590 nm. These two absorption acromions strengthen slightly after thermal annealing for 10 min. The intensity of the two acromions indirectly represents the degree of ordered aggregation of molecular chains, consistent with the intensity of the alkyl-stacking (100). Different from P3HT, the maximum absorption peak of ZY-4Cl redshifts by 20 nm from 695 to 705 nm after thermally annealing the as-cast neat film for 10 min. This indicates that the aggregation of ZY-4Cl is more intense than that of P3HT after annealing.

Subsequently, we acquired the UV-vis absorption spectra of the blend films at different annealing times. As shown in Fig. 4b, an absorption acromion appeared at 635 nm after thermal annealing for 10 s. The absorption edge gradually redshifted with annealing in the beginning and it no longer redshifted after 30 s. Generally, V_{OC} depends on the difference in energy levels between the HOMO of the donor and the lowest unoccupied molecular orbital (LUMO) of the acceptor.[55] The narrowed bandgap leads to a rapid decrease in V_{OC}, which resulted from the redshift spectra of the crystallized acceptor. The crystallinity of P3HT is enhanced a little after annealing treatment, which will further increase the HOMO of P3HT, leading to a slow V_{OC} drop after annealing for 30 s.

The blend films obtained after thermal annealing for 30 s to 1 h showed very analogous absorption profiles, but the absorption peak intensity changed slightly. We recorded the absorption coefficients at ~560 and ~700 nm to monitor the degree of ordered aggregation of P3HT chains and ZY-4Cl molecules in the blend system. The absorption peaks at ~560 nm correspond to P3HT and the signals at ~700 nm originate from ZY-4Cl. As shown in Fig. 4c and Table S5,† the P3HT chain ordered aggregation increases rapidly with annealing, as signaled by the sudden increase of the absorption peak intensity upon thermal annealing for 5 s. Subsequently, the absorption peak intensity becomes steady, indicating that the molecular chains are no longer aggregated visibly. Meanwhile, the absorption peaks of ZY-4Cl increase to the maximum at 30 s and then decrease gradually, which indicated that the crystallization of ZY-4Cl molecules strengthens the absorption intensity fast in a short annealing time and then the agglomeration of ZY-4Cl hinders the absorption.

2.5. Charge separation and transport behaviors

In order to explore the influence of molecular packing and microstructural details on device performance, we carried out further research on charge separation and transport behaviors of devices. The analysis of photocurrent density (J_{ph}) *versus* effective voltage (V_{eff}) was performed to study the exciton

dissociation processes in the devices. J_{ph} is the difference between the current density in the dark and under illumination, V_{eff} is the difference between the voltage when J_{ph} is zero and the applied voltage. The exciton dissociation probability (P_{diss}) is defined as the ratio of J_{ph}/J_{sat} (J_{sat} represents the saturation current density). As shown in Fig. 4d and Table S6,† the J_{ph} of the as-cast device linearly increases with the voltage and cannot be fully saturated even at high V_{eff}. Thus, the device shows a very low P_{diss} of 11.9%. This result shows that the charge separation is hindered severely. In contrast, the J_{ph} of the devices annealed for more than 10 s saturates well at a low V_{eff}. As a result, all the devices annealed for over 10 s show P_{diss} values above 90%. This is due to the completion of the acceptor crystallization forming a good interpenetrating network with appropriate phase separation. Such effective exciton dissociation will rapidly increase the current of the annealed films. The sudden increase in J_{SC} within 30 s is due to enhanced photon absorption and increased exciton dissociation. In Fig. S8,† the photoluminescence (PL) of P3HT is quenched sufficiently in the as-cast blend films, suggesting that the charge transfer in the blends is very efficient. This can be well explained by the small domains and well-mixed morphology. The efficiency of charge dissociation gradually decreases with the annealing time, which matches the varying trend of domain sizes (Fig. S6b†).

The competition between charge recombination and extraction is directly related to the FF of bulk-heterojunction solar cells.[56,57] We first measured the J_{SC} of devices under varying light intensity (P_{light}) to analyze the charge recombination behavior (Fig. S9†). It has been demonstrated that the slope (α) of J_{SC} *versus* P_{light} can provide insight into bimolecular recombination. The relation can be expressed as $J_{SC} \propto P_{light}^{\alpha}$, where weak bimolecular recombination would lead to a linear dependence with the exponential factor α value approaching 1. The α values of all devices are summarized in Table S7.† As shown in Fig. 4e, all of the devices herein show a linear dependence of J_{SC} on P_{light} with a slope above 0.95 and the α value first increases and then decreases slightly with annealing time. The low α value of the as-cast device should be attributed to a low carrier density due to the low P_{diss}, which explains the lowest J_{SC} and FF. This indicates that bimolecular recombination is minimized with a short period of annealing and longer annealing will increase bimolecular recombination again. The correlation between V_{OC} and P_{light} can be expressed as $V_{OC} = \beta(kT/e)\ln(P_{light}) + c$, where k is the Boltzmann constant, T is the temperature, e is the elementary charge, c is a constant, and β is the scaling factor. Typically, a slope of 1 kT/e illustrates that bimolecular recombination is the dominating mechanism. In contrast, a slope of 2 kT/e indicates that trap-assisted recombination is the dominating mechanism. The degree of trap-assisted recombination with annealing time shows the same trend as bimolecular recombination. All the devices demonstrate a recombination mechanism of bimolecular and trap-assisted processes under open-circuit conditions.

Subsequently, we investigated the charge carrier transport properties of the devices using the space charge limited current (SCLC) model.[58] We adopted the hole-only (ITO/PEDOT:PSS/P3HT:ZY-4Cl/MoO_3/Al) and electron-only (ITO/ZnO/P3HT:ZY-4Cl/Al) device configurations and the mobility data are shown in Fig. S10 and Table S8.† The evolution plots of hole mobility and electron mobility as a function of annealing time are expressed in Fig. 4f. The hole and electron mobilities have an instant jump (from $\sim 10^{-5}$ to $\sim 10^{-4}$ $cm^2\ V^{-1}\ s^{-1}$) at the beginning of annealing, which is due to the significantly enhanced crystallinity of P3HT and the formation of ZY-4Cl crystals. Then both mobilities increase slightly as the crystallinity of the donor and acceptor increases slowly with annealing in the first 1 min. When the annealing time exceeds 1 min, the electron mobility decreases slightly. Meanwhile, unexpectedly, the hole mobility continues to increase with annealing, and it reaches 1.91×10^{-3} $cm^2\ V^{-1}\ s^{-1}$ after 1 h of annealing. Different from small molecule acceptors, long-chain conjugated polymer P3HT cannot move over large distances, due to its wide distribution area and the constrained dynamics. Thermal annealing can enhance the crystallinity of polymer chains, but cannot greatly change their overall spatial distribution. The agglomeration of ZY-4Cl crystals causes large-scale domains of the acceptor in the blend films. Correspondingly, the place where the acceptor has moved will offer the donors a larger crystallization area, which will cause a larger-scale domain and stronger crystallinity of the donor. Therefore, the hole transport channel composed of the larger donor domain of the polymer molecule within the whole space is still very intact and interconnected. As the L_c of the (100) alkyl-stacking direction increases, the interaction of polymer chains is also increased, generating more conjugated π–π electrons. This also dramatically increases the hole mobility. Unfortunately, the degree of imbalance in charge carrier transport, expressed by the ratio of hole and electron mobility (μ_h/μ_e), is greater than 1 and increases rapidly when the annealing time exceeds 1 min. The high asymmetry of μ_h and μ_e also makes the current reduce more obviously.

Consequently, based on all the results above, the device efficiency first increases rapidly and then decreases slowly. We note that the rapid improvement of PCE is not due to the removal of solvent (Fig. S11 and Table S9†) but rather better charge separation and transport within the thin film. Similar phenomena can be found with CF and CB as processing solvents as shown in Fig. S12 and Table S10.† Interestingly, the short thermal treatment appears to be effective for this system, regardless of the boiling points of cast solvents. Much higher efficiency can be achieved in a very short time (30 s) than that of the film normally annealed for 10 min, which is of great significance to the improvement of production efficiency for OPV commercial applications.

2.6. Evolution diagram and microstructure–performance relationships

Combining all the above analysis, we can infer the microstructure evolution of the P3HT:ZY-4Cl blend film during the heating process. Such results demonstrate a good correlation between molecular packing, morphology details and device performance. The schematic diagrams of time-dependent evolution of crystallization and phase separation during the thermal annealing process in this system are shown in Fig. 5a.

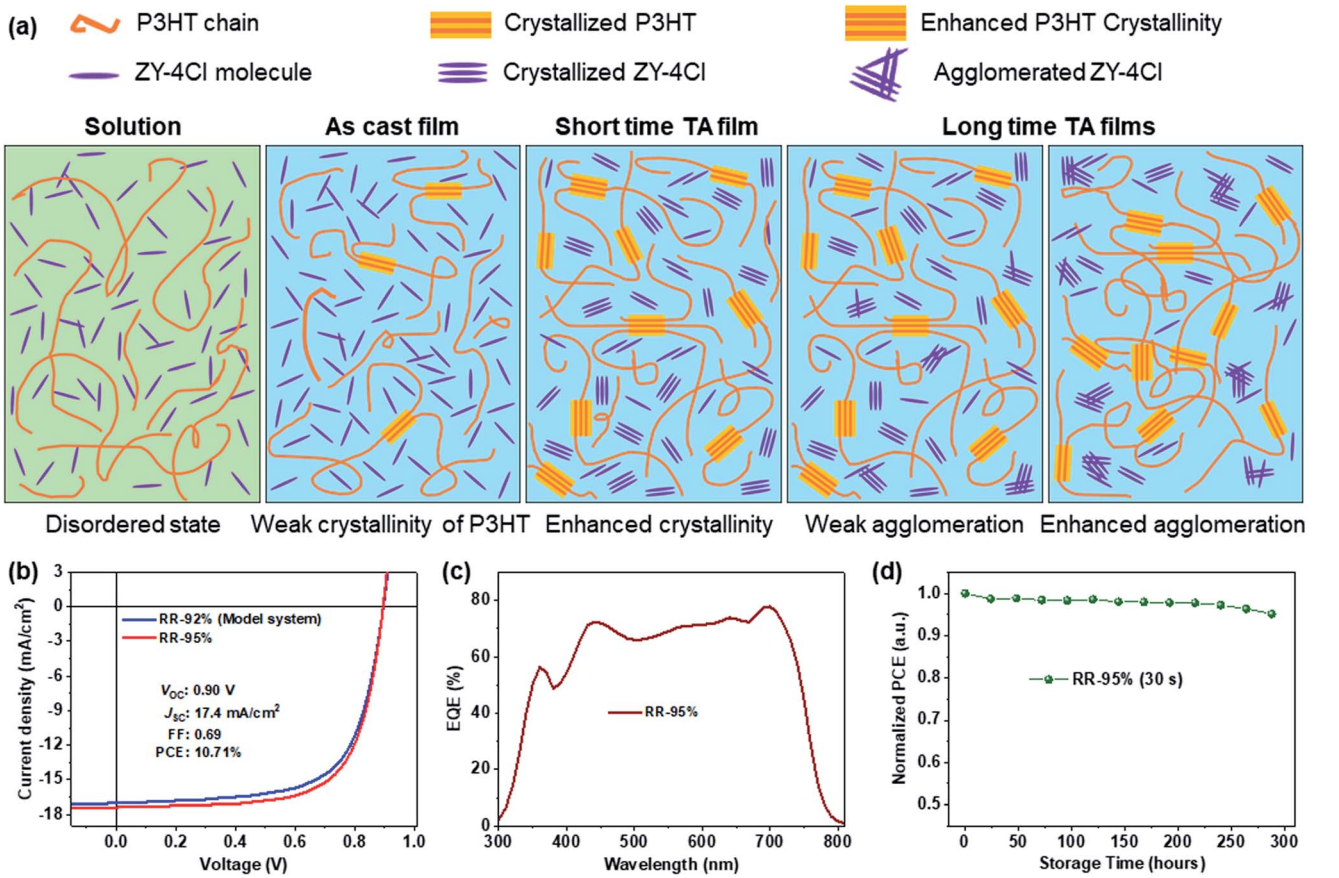

Fig. 5 (a) The schematic diagrams of time-dependent evolution of crystallization and phase separation of the model polythiophene:nonfullerene blend during the thermal annealing process. (b) Optimized *J*–*V* characteristics of a new P3HT batch with 95% regioregularity and (c) the corresponding EQE spectrum. (d) Normalized PCE of the optimized device *versus* the storage time.

In the hot solution, conjugated P3HT polymer molecule chains and small molecule acceptors ZY-4Cl are freely distributed in a disordered state over a large space. Along with the solution spin-coating into blend films, the solvent volatilization causes randomly curled polymer chains to quickly aggregate and produce a low extent of crystallization. ZY-4Cl molecules are mixed into the P3HT chains, which caused most of the P3HT to be in a disordered state. Moreover, ZY-4Cl molecules are in a freely distributed amorphous state within the entire as-cast film space. The tiny phase separation makes the film interface of the donor and acceptor not clear and unable to form a continuous charge transporting channel.

As shown in Fig. S13 and Table S11,† when the annealing temperature is lower than 100 °C, the PCE gradually increased with the TA time, while the maximum PCE is still no more than 5%. When the annealing temperature increases (for instance, >100 °C), the maximum PCEs can be quickly reached in a short period. As the annealing temperature (130 °C) is above the glass transition temperature (T_g) of the materials (see Fig. S14†), the acceptor molecules may transition from a disordered amorphous state to an ordered crystalline state rapidly through thermal activation. At the same time, the polymer chains can also form a more ordered packing, which is conducive to building an interpenetrating network structure. The phase separation of the active blends is optimized with the quickly enhanced crystallinity, which significantly improved the P_{diss}, mobilities and phase purity of mixed domains. Hence, the highest PCE is obtained with annealing for a short time. Furthermore, we achieved a significantly higher PCE of 10.71% with a V_{OC} of 0.90 V, a J_{SC} of 17.4 mA cm^{-2} and a FF of 0.69 by using a new batch of P3HT with higher regioregularity, detailed data of which can be found in Fig. 5b and Table 1, and the corresponding EQE spectrum is shown in Fig. 5c. This is the highest efficiency among P3HT-based organic photovoltaic cells at present (see Fig. 1a). Note that the best-performing cell also exhibited excellent storage stability, as shown in Fig. 5d.

With even longer annealing time, heat drives the acceptors to move freely over a larger space, causing them to start to agglomerate due to Ostwald ripening. This kind of agglomeration is very chaotic and disordered compared to crystallization. Larger domains result in a higher extent of phase separation and a slightly lower efficiency. When annealing for a long time, the excessive thermal energy will accelerate the diffusion of acceptors and create many island-like agglomerations of acceptors. The fracture of the large acceptor domains causes a slight decrease in electron mobility. In contrast, long-chain polymer donors with limited kinetics can only move locally, so the donor transport channel is still continuous and

distributed over a wide area. Further enhanced crystallinity dramatically increases hole mobility. Consequently, the carrier transport becomes more unbalanced and the phase separation becomes more intense. The intermolecular interaction between the donor and acceptor is so strong that it destroys the interpenetrating network structure that has been formed. This leads to reduced P_{diss} and stronger recombination, resulting in a significant drop in the device efficiency. This suggests a fast thermally activated kinetic process for the improvement in device performance. Though the crystallization of P3HT and ZY-4Cl contributes to the improvement of device performance, the crystallization of ZY-4Cl plays a dominant role. The significantly improved PCE after annealing for 30 s mainly originated from the improved crystallinity of ZY-4Cl and appropriate phase separation of the P3HT:ZY-4Cl blend. The stability under thermal stress[59] will be the next focus of these polythiophene solar cells.

3. Conclusion

In the present study, we were able to precisely tune the crystalline order and improve the device efficiency of a representative P3HT:nonfullerene photovoltaic blend and importantly identify the key influential factors in governing the photovoltaic behaviors of the blend over the course of thermal annealing. For the blend system made of P3HT and ZY-4Cl, we have disclosed the time-dependent evolution of phase separation, crystallization and photovoltaic properties during the thermal annealing process. It was found that the acceptor crystallized and then agglomerated rapidly with the extension of annealing time, while the crystallization of P3HT improved slightly after annealing and exhibited no change of crystal form. As a result, the phase separation of the blend films gradually increases with the annealing time, which leads to the device efficiency first increasing rapidly and then decreasing slowly.

Interestingly, after only 30 s of thermal annealing, we achieved an impressive PCE of 10.71%, which is the first time that a PCE of more than 10% is reported in P3HT-based OPV cells without using any additive and sets a new efficiency record for P3HT-OPVs. This is significantly higher than the efficiency of conventional annealing for 10 min (9.37%) and approximately 20 times as high as that of the as-cast device (0.51%). This work suggests that delicately controlling the crystallization order and sequence of both the donor and acceptor is crucial to the performance optimization of P3HT-OPVs. This knowledge may allow us to guide the quick selection of the best processing conditions and fabricate efficient and cost-effective optoelectronic devices. Undoubtedly, performing real-time investigations of crystallization and phase transitions can aid in obtaining a fundamental understanding of the influence of processing parameters in these critically important and low-cost material systems.

4. Experimental section

4.1. Materials

PEDOT:PSS (4083) was purchased from Clevios™. PDINO was purchased from Derthon Optoelectronic Materials Science Technology Co. Ltd. All solvents were purchased from Sigma Aldrich or Heowns. P3HT was from the same P-26K batch with 92% regioregularity used in our previous work.[42] ZY-4Cl was synthesized according to the procedures previously reported.[28] Other experimental and instrumental details can be found in the ESI.†

4.2. Device fabrication

Devices were fabricated with the conventional device structure of ITO/PEDOT:PSS/P3HT:ZY-4Cl/PDINO/Al. P3HT:ZY-4Cl was dissolved in THF at a total concentration of 15 mg mL^{-1} and the optimal D/A ratio was 1 : 1 (w/w). To fully dissolve P3HT and ZY-4Cl, blend solutions were stirred at 50 °C for 4 h. PDINO was dissolved in methanol at a concentration of 1.5 mg mL^{-1}. Devices were fabricated as follows. Firstly, the ITO substrates were treated with UV ozone for 25 min. Then, about 20 nm PEDOT:PSS layers were spin-coated on the pre-cleaned ITO substrates and annealed at 150 °C for 20 min. Subsequently, the substrates were transferred to an argon-filled glovebox. The mixed solutions were spin-coated onto the PEDOT:PSS layers, and the thicknesses of all active layers were about 100 nm. Then the films were treated with thermal annealing at 130 °C for different times. PDINO was spin-coated on the top of the active layers. Finally, 100 nm-thick Al was deposited on the top of the PDINO layer under high vacuum. The effective area of the P3HT-OPV cells is about 0.04 cm^2.

Author contributions

Long Ye and Kaihu Xian conceived the idea and designed the experimental protocols. Kaihu Xian performed the device fabrication and characterization, analyzed the data and wrote the original draft. Yang Liu supplied the photovoltaic materials. Junwei Liu, Zhongxiang Peng, Kangkang Zhou, Mengyuan Gao and Jidong Zhang performed the GIWAXS and DSC data acquisition. Jinde Yu, Yifan Xing and Guanghao Lu conducted the *in situ* film-depth-dependent light absorption spectroscopy (FLAS) measurements. Yanhou Geng, Jianhui Hou, and Wenchao Zhao participated in the discussion and manuscript editing. Long Ye directed the whole research. All authors reviewed the manuscript.

Conflicts of interest

The authors declare that they have no known competing financial interests or personal relationships that could have appeared to influence the work reported in this paper.

Acknowledgements

This work was made possible thanks to the financial supports of the open research fund of the Songshan Lake Materials Laboratory (No. 2021SLABFN20) and the National Natural Science Foundation of China (No. 52073207 and No. 52121002). L. Ye also appreciates the State Key Laboratory of Applied Optics (No. SKLAO2021001A17) and the Peiyang Scholar Program of Tianjin

University for support. G. Lu acknowledges the support from the Key Scientific and Technological Innovation Team Project of Shaanxi Province (2020TD-002). J.H. acknowledges the support from the National Key Research and Development Program of China (2019YFA0705900) funded by MOST and the Basic and Applied Basic Research Major Program of Guangdong Province (2019B030302007). GIWAXS data acquisition at beamline BL14B1 of the Shanghai Synchrotron Radiation Facility and beamline 1W1A of the Beijing Synchrotron Radiation Facility is deeply appreciated.

References

1 O. Inganas, *Adv. Mater.*, 2018, **30**, 1800388.
2 F. C. Krebs, *Sol. Energy Mater. Sol. Cells*, 2009, **93**, 394–412.
3 Z. Peng, K. Xian, Y. Cui, Q. Qi, J. Liu, Y. Xu, Y. Chai, C. Yang, J. Hou, Y. Geng and L. Ye, *Adv. Mater.*, 2021, **33**, 2106732.
4 H. Kang, G. Kim, J. Kim, S. Kwon, H. Kim and K. Lee, *Adv. Mater.*, 2016, **28**, 7821–7861.
5 C. Xu, K. Jin, Z. Xiao, Z. Zhao, X. Ma, X. Wang, J. Li, W. Xu, S. Zhang, L. Ding and F. Zhang, *Adv. Funct. Mater.*, 2021, **31**, 2107934.
6 M. Zhang, L. Zhu, G. Zhou, T. Hao, C. Qiu, Z. Zhao, Q. Hu, B. W. Larson, H. Zhu, Z. Ma, Z. Tang, W. Feng, Y. Zhang, T. P. Russell and F. Liu, *Nat. Commun.*, 2021, **12**, 309.
7 S. Chen, L. Feng, T. Jia, J. Jing, Z. Hu, K. Zhang and F. Huang, *Sci. China: Chem.*, 2021, **64**, 1192–1199.
8 Y. Li, Y. Cai, Y. Xie, J. Song, H. Wu, Z. Tang, J. Zhang, F. Huang and Y. Sun, *Energy Environ. Sci.*, 2021, **14**, 5009–5016.
9 Y. Qin, Y. Chang, X. Zhu, X. Gu, L. Guo, Y. Zhang, Q. Wang, J. Zhang, X. Zhang, X. Liu, K. Lu, E. Zhou, Z. Wei and X. Sun, *Nano Today*, 2021, **41**, 101289.
10 B. Fan, M. Li, D. Zhang, W. Zhong, L. Ying, Z. Zeng, K. An, Z. Huang, L. Shi, G. C. Bazan, F. Huang and Y. Cao, *ACS Energy Lett.*, 2020, **5**, 2087–2094.
11 L.-W. Feng, J. Chen, S. Mukherjee, V. K. Sangwan, W. Huang, Y. Chen, D. Zheng, J. W. Strzalka, G. Wang, M. C. Hersam, D. DeLongchamp, A. Facchetti and T. J. Marks, *ACS Energy Lett.*, 2020, **5**, 1780–1787.
12 J. Yuan, Y. Zhang, L. Zhou, G. Zhang, H.-L. Yip, T.-K. Lau, X. Lu, C. Zhu, H. Peng, P. A. Johnson, M. Leclerc, Y. Cao, J. Ulanski, Y. Li and Y. Zou, *Joule*, 2019, **3**, 1140–1151.
13 J. Xiao, X. Jia, C. Duan, F. Huang, H. L. Yip and Y. Cao, *Adv. Mater.*, 2021, **33**, 2008158.
14 C. J. Brabec, S. Gowrisanker, J. J. M. Halls, D. Laird, S. J. Jia and S. P. Williams, *Adv. Mater.*, 2010, **22**, 3839–3856.
15 E. Wang, L. Hou, Z. Wang, S. Hellstrom, F. Zhang, O. Inganas and M. R. Andersson, *Adv. Mater.*, 2010, **22**, 5240–5244.
16 C. Sun, F. Pan, S. Chen, R. Wang, R. Sun, Z. Shang, B. Qiu, J. Min, M. Lv, L. Meng, C. Zhang, M. Xiao, C. Yang and Y. Li, *Adv. Mater.*, 2019, **31**, 1905480.
17 Z. a. Li, C.-C. Chueh and A. K. Y. Jen, *Prog. Polym. Sci.*, 2019, **99**, 101175.
18 T. M. Pappenfus, F. Almyahi, N. A. Cooling, E. W. Culver, S. C. Rasmussen and P. C. Dastoor, *Macromol. Chem. Phys.*, 2018, **219**, 1800272.
19 J. R. Pouliot, F. Grenier, J. T. Blaskovits, S. Beaupre and M. Leclerc, *Chem. Rev.*, 2016, **116**, 14225–14274.
20 Y. Liu, K. Xian, R. Gui, K. Zhou, J. Liu, M. Gao, W. Zhao, X. Jiao, Y. Deng, H. Yin, Y. Geng and L. Ye, *Macromolecules*, 2022, **55**, 133–145.
21 A. Marrocchi, D. Lanari, A. Facchetti and L. Vaccaro, *Energy Environ. Sci.*, 2012, **5**, 8457–8474.
22 A. Facchetti, L. Vaccaro and A. Marrocchi, *Angew. Chem., Int. Ed.*, 2012, **51**, 3520–3523.
23 X. Guo, C. Cui, M. Zhang, L. Huo, Y. Huang, J. Hou and Y. Li, *Energy Environ. Sci.*, 2012, **5**, 7943–7949.
24 Y. Qin, M. A. Uddin, Y. Chen, B. Jang, K. Zhao, Z. Zheng, R. Yu, T. J. Shin, H. Y. Woo and J. Hou, *Adv. Mater.*, 2016, **28**, 9416–9422.
25 S. Chatterjee, S. Jinnai and Y. Ie, *J. Mater. Chem. A*, 2021, **9**, 18857–18886.
26 Q. Liang, X. Jiao, Y. Yan, Z. Xie, G. Lu, J. Liu and Y. Han, *Adv. Funct. Mater.*, 2019, **29**, 1807591.
27 X. Xu, G. Zhang, L. Yu, R. Li and Q. Peng, *Adv. Mater.*, 2019, **31**, 1906045.
28 C. Yang, S. Zhang, J. Ren, M. Gao, P. Bi, L. Ye and J. Hou, *Energy Environ. Sci.*, 2020, **13**, 2864–2869.
29 E. Pascual-San-José, X. Rodríguez-Martínez, R. Adel-Abdelaleim, M. Stella, E. Martínez-Ferrero and M. Campoy-Quiles, *J. Mater. Chem. A*, 2019, **7**, 20369–20382.
30 J.-T. Chen and C.-S. Hsu, *Polym. Chem.*, 2011, **2**, 2707–2722.
31 Y. Yoshimoto, S. Sugiyama, S. Shimada, T. Kaneko, S. Takagi and I. Kinefuchi, *Macromolecules*, 2021, **54**, 958–969.
32 L. Ye, H. Ke and Y. Liu, *Trends Chem.*, 2021, **3**, 1074–1087.
33 K. Xian, Y. Cui, Y. Xu, T. Zhang, L. Hong, H. Yao, C. An and J. Hou, *J. Phys. Chem. C*, 2020, **124**, 7691–7698.
34 M. Gao, W. Wang, J. Hou and L. Ye, *Aggregate*, 2021, **2**, e46.
35 W. Xu, X. Ma, J. H. Son, S. Y. Jeong, L. Niu, C. Xu, S. Zhang, Z. Zhou, J. Gao, H. Y. Woo, J. Zhang, J. Wang and F. Zhang, *Small*, 2021, **17**, 2104215.
36 S. Holliday, R. S. Ashraf, C. B. Nielsen, M. Kirkus, J. A. Rohr, C. H. Tan, E. Collado-Fregoso, A. C. Knall, J. R. Durrant, J. Nelson and I. McCulloch, *J. Am. Chem. Soc.*, 2015, **137**, 898–904.
37 S. Holliday, R. S. Ashraf, A. Wadsworth, D. Baran, S. A. Yousaf, C. B. Nielsen, C. H. Tan, S. D. Dimitrov, Z. Shang, N. Gasparini, M. Alamoudi, F. Laquai, C. J. Brabec, A. Salleo, J. R. Durrant and I. McCulloch, *Nat. Commun.*, 2016, **7**, 11585.
38 C. Yang, R. Yu, C. Liu, H. Li, S. Zhang and J. Hou, *ChemSusChem*, 2021, **14**, 1–8.
39 M. Osaka, D. Mori, H. Benten, H. Ogawa, H. Ohkita and S. Ito, *ACS Appl. Mater. Interfaces*, 2017, **9**, 15615–15622.
40 Z. Wang, K. Gao, Y. Kan, M. Zhang, C. Qiu, L. Zhu, Z. Zhao, X. Peng, W. Feng, Z. Qian, X. Gu, A. K. Jen, B. Z. Tang, Y. Cao, Y. Zhang and F. Liu, *Nat. Commun.*, 2021, **12**, 332.
41 Q. Liang, J. Han, C. Song, X. Yu, D.-M. Smilgies, K. Zhao, J. Liu and Y. Han, *J. Mater. Chem. A*, 2018, **6**, 15610–15620.
42 Y. Liu, K. Xian, Z. Peng, M. Gao, Y. Shi, Y. Deng, Y. Geng and L. Ye, *J. Mater. Chem. A*, 2021, **9**, 19874–19885.
43 J. Liu, Y. Sun, X. Gao, R. Xing, L. Zheng, S. Wu, Y. Geng and Y. Han, *Langmuir*, 2011, **27**, 4212–4219.

44 A. L. Patterson, *Phys. Rev.*, 1939, **56**, 978–982.
45 S. Marina, A. D. Scaccabarozzi, E. Gutierrez-Fernandez, E. Solano, A. Khirbat, L. Ciammaruchi, A. Iturrospe, A. Balzer, L. Yu, E. Gabirondo, X. Monnier, H. Sardon, T. D. Anthopoulos, M. Caironi, M. Campoy-Quiles, C. Müller, D. Cangialosi, N. Stingelin and J. Martin, *Adv. Funct. Mater.*, 2021, **31**, 2103784.
46 L. Zhu, M. Zhang, G. Zhou, T. Hao, J. Xu, J. Wang, C. Qiu, N. Prine, J. Ali, W. Feng, X. Gu, Z. Ma, Z. Tang, H. Zhu, L. Ying, Y. Zhang and F. Liu, *Adv. Energy Mater.*, 2020, **10**, 1904234.
47 L. Yu, D. Qian, S. Marina, F. A. A. Nugroho, A. Sharma, S. Hultmark, A. I. Hofmann, R. Kroon, J. Benduhn, D. M. Smilgies, K. Vandewal, M. R. Andersson, C. Langhammer, J. Martin, F. Gao and C. Muller, *ACS Appl. Mater. Interfaces*, 2019, **11**, 21766–21774.
48 L. Ye, Y. Xiong, M. Zhang, X. Guo, H. Guan, Y. Zou and H. Ade, *Nano Energy*, 2020, **77**, 105310.
49 L. Ye, X. Jiao, M. Zhou, S. Zhang, H. Yao, W. Zhao, A. Xia, H. Ade and J. Hou, *Adv. Mater.*, 2015, **27**, 6046–6054.
50 L. Ye, Y. Xiong, S. Li, M. Ghasemi, N. Balar, J. Turner, A. Gadisa, J. Hou, B. T. O'Connor and H. Ade, *Adv. Funct. Mater.*, 2017, **27**, 1702016.
51 Z. Xu, L.-M. Chen, G. Yang, C.-H. Huang, J. Hou, Y. Wu, G. Li, C.-S. Hsu and Y. Yang, *Adv. Funct. Mater.*, 2009, **19**, 1227–1234.
52 P. G. Karagiannidis, D. Georgiou, C. Pitsalidis, A. Laskarakis and S. Logothetidis, *Mater. Chem. Phys.*, 2011, **129**, 1207–1213.
53 T. Xiao, J. Wang, S. Yang, Y. Zhu, D. Li, Z. Wang, S. Feng, L. Bu, X. Zhan and G. Lu, *J. Mater. Chem. A*, 2020, **8**, 401–411.
54 P. W. Voorhees, *J. Stat. Phys.*, 1984, **38**, 231–252.
55 S. Sweetnam, K. R. Graham, G. O. Ngongang Ndjawa, T. Heumuller, J. A. Bartelt, T. M. Burke, W. Li, W. You, A. Amassian and M. D. McGehee, *J. Am. Chem. Soc.*, 2014, **136**, 14078–14088.
56 D. Bartesaghi, I. d. C. Pérez, J. Kniepert, S. Roland, M. Turbiez, D. Neher and L. J. A. Koster, *Nat. Commun.*, 2015, **6**, 7083.
57 L. Dou, J. You, Z. Hong, Z. Xu, G. Li, R. A. Street and Y. Yang, *Adv. Mater.*, 2013, **25**, 6642–6671.
58 O. G. Reid, K. Munechika and D. S. Ginger, *Nano Lett.*, 2008, **8**, 1602–1609.
59 L. Ye, M. Gao and J. Hou, *Sci. China: Chem.*, 2021, **64**, 1875–1887.